

Analysis and Design of 3 kW Axial Flux Permanent Magnet Synchronous Motor for Electric Car

G. R. Bruzanga , A. J. Sguarezi Filho  *Senior Member, IEEE* and A. Pelizari 

Abstract—Axial flux topology machines are extremely advantageous when used in electric vehicles. The machine design of this topology presents some challenges, considering that it must meet the vehicle's and track's prerequisites. This work presents a design methodology for axial flux machines focusing on electrical traction based on the comparison between the analytical and computational resolution by the finite element method.

Based on the pre-established resistant torque and power, as well as the rated data of the vehicle, an analytical method is used that allows the determination of the main parameters of a permanent magnets axial flux machine. Then, the principle of magnetic circuit theory was applied to determine the flux densities in the ferromagnetic material of the armature, rotor, permanent magnets and air gap, the latter, as a starting point, is adopted at its maximum value and from this, the flux densities on other parts of the machine are estimated. After flux densities estimation, it is verified that the induction levels achieved are under the saturation induction level in ferromagnetic material, enabling the development of a model in computational simulation software with numerical resolution by the finite element method Ansys Maxwell® in magnetostatic regime. Once the simulation was done, the inductions were compared with those obtained by analytical method. It is verified that the absolute errors obtained between the two methods present values less than 10%, resulting in the construction of a 3 kW prototype for installation in a vehicle for educational purposes. The bench tests carried out on the prototype and the test on the track up to the adopted maximum limit speed indicated that the torque results reached the prerequisites of 30 km/h on the track.

Index Terms—Axial Flux Motor, Finite Element Method, PMSM, Electric Vehicle.

I. INTRODUCTION

One of the main uses of electric motors in recent decades has been in vehicle traction systems [1]. In such applications, an alternative is the use of machines with different topologies [2] that not only address the issue of physical space but also increase the power density, among them, the axial flux topology machines [3], [4]. One of the main advantages of this topology is the physical space it occupies [5], [6], since its axial length is shortened compared to radial flux topology machines [7], in addition to the fact that they have higher power and torque densities [8], [9] when the space is limited. In addition, the axial flux machines has some advantages as robustness and compact shape. The magnets are manufactured with flat surfaces. In such machines the air gap can be adjusted during and after the assembly step. Besides the fact the possibility of using several modules on the same drive

axle. In another hand, some disadvantages as compromised structural stability due to the size of the discs [10]. Also due to the large discs, they have a high moment of inertia. Another issue is that the contact surface between rotor and shaft does not increase proportionally with its output power, increasing the possibility of vibration, being one of the main causes of failures in disk-type motors.

II. ASPECTS OF AXIAL AND RADIAL MACHINES

The axial flux brushless permanent magnet machines (AFBPM), also known as disk-type machines, are only preferably used in situations where the axial space is limited, specially inside the wheels in electric cars. Regarding the number of disks, the most common topologies are single-sided, double-sided or multi-stage. Fig 1 shows the classification of axial flux machines in terms of number of discs:

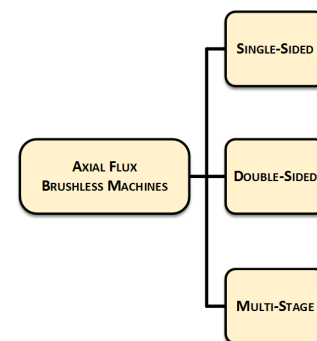


Fig. 1. Classification of AFBPM Machines.

In these topologies, the ease of assembly of the magnets stands out, since they are manufactured with flat surfaces and, due to the fact that the air gap is flat, it allows its distance adjustment during and after assembly. Due to the large discs, the structural stability is slightly lower compared to radial machines. Single-sided machines (SSAFBPM) have a simpler construction of the 3 arrangements, however, they have lower torque capacity compared to double-sided machines (DSAFBPM). The DSAFBPM machines feature twice the power and the attraction forces between stator and rotor are balanced. Another advantage is the possibility of redundancy when connected in parallel, where one stator can work even if the other disc fails. Multi-stage machines (MSAFBPM), are normally used on machines with power in the range of 300 kW or more and, since the machine power varies depending on the radius of the disk, this increase must be limited by inserting

G. R. Bruzanga, A. J. Sguarezi Filho and A. Pelizari are with the Universidade Federal do ABC - UFABC, Brazil. e-mails: gabriel.bruzanga@ufabc.edu.br, alfeu.sguarezi@ufabc.edu.br and ademar.pelizari@ufabc.edu.br

more discs, for stability issues, mainly in the mechanical joints between disc-shaft and the axial force suffered by the bearings.

To solve the space issue, particularly in vehicular electric traction, the AFBPM machines has several assembly possibilities, regarding the position of the electric machine to the traction system. Depending on the available space and the power required, these possibilities are shown in Fig.2:

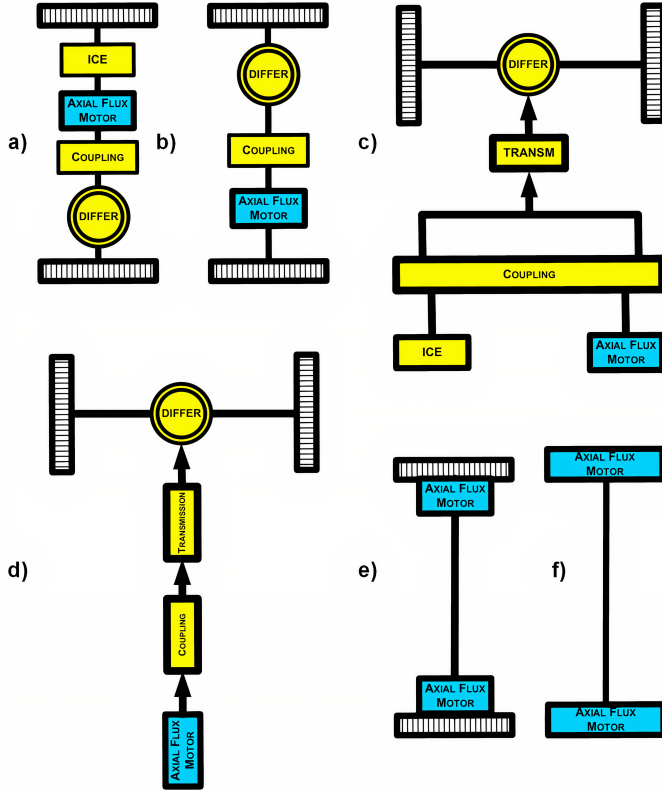


Fig. 2. Installation options for AFBPM motors.

The table I shows the main dimensions and characteristics of a machine of the same power, speed, voltage, and frequency range as a commonly sold motor compared to the SSAFBPM machine in this project.

TABLE I
COMPARISON BETWEEN AXIAL AND RADIAL FLUX MACHINES

Quantity	Axial	Radial
Rated Power [kW]	3	3
Rated Voltage [V]	220	220
Rated Speed [rpm]	1200	1150
Number of Poles	6	6
Rated Frequency [Hz]	60	60
Rated Current [A]	8,75	12,6
Service Factor	1,00	1,15
Efficiency [%]	90	83
Motor Mass [kg]	27,0	41,2
Motor Diameter [m]	0,26	0,21
Motor Length [m]	0,15	0,39
Power Density [W/kg]	111,1	72,8
Torque-Current Ratio [N.m/A]	1,22	0,97

In terms of mechanical power, the axial-flux machine with toroidal armature compared to the conventional radial-flux machine for applications with limited axial length is more

convenient. In situations with high mechanical load, it has a higher torque than both transverse-flux (TFBPM) and radial-flux (RFBPM) machines over a wide speed range and with high efficiency [11], [12].

III. ANALYTICAL METHOD FLOWCHART

Fig. 3 shows the main steps of the methodology adopted to the analytical method, where the blocks of the flowchart represent the calculations and assumptions from the nominal values of the track, the vehicle and the implementation of the theory of magnetic circuits, that were considered the core of the method.

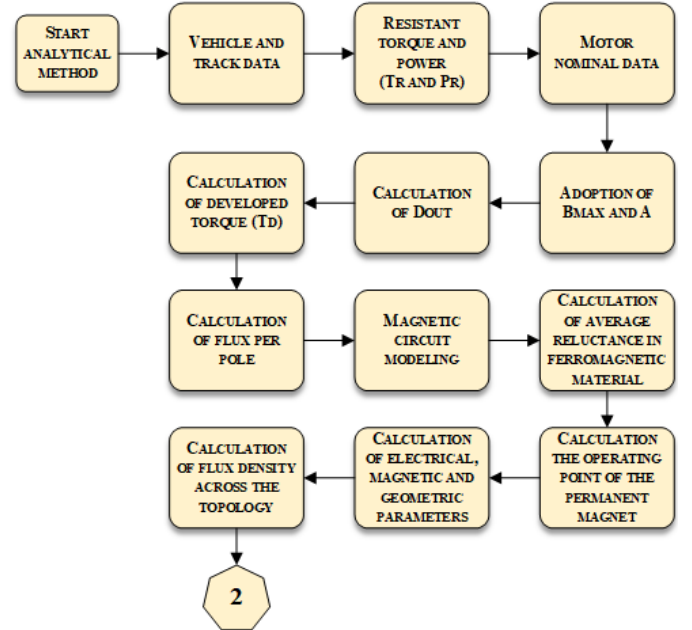


Fig. 3. Flowchart of Analytical Method.

IV. TRACK RESISTANT POWER AND TORQUE

At the traction sizing stage, it is essential that the power of the electric machine is not under or oversized [13] by the already mentioned limiting factors, and also taking into account the condition of the track [14]. Thus, the resistant force, power and torque required for the SSAFBPM machine design were calculated, in order to meet the pre-established runway conditions [15], such as aerodynamic drag, the coefficient of friction and the slope. For this purpose, the diagram of forces acting on the vehicle was used, as shown in Fig. 4.

It can be observed the resulting force in the direction of the longitudinal axis x :

$$F_R = F_{ad} + F_{rr} + F_{Incl} + F_{accel} \quad (1)$$

In (1) F_R is the resistant force resulting from the movement of the vehicle, F_{ad} is the aerodynamic drag resistant force, F_{rr} is the friction resistant force of the tires, F_{Incl} is the resistant force due to the slope of the track and F_{accel} is the force due to the vehicle acceleration, all in N . Recall that the aerodynamic drag force can be determined by:

$$F_{ad} = \rho_{ar} \cdot A_f \cdot C_d \cdot (V_x \pm V_{wind})^2 \quad (2)$$

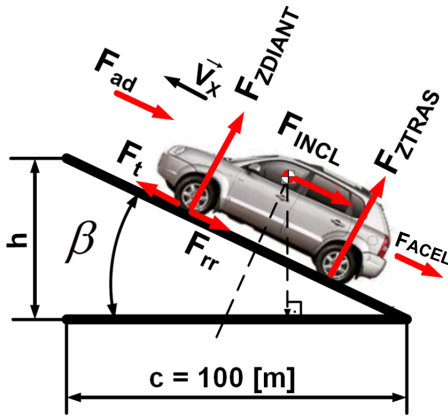


Fig. 4. Forces Acting on the Vehicle.

The ρ_{ar} , in (2), is the air density in kg/m^3 , A_f is the front area of the vehicle in m^2 , C_d is the aerodynamic drag coefficient, V_x is the vehicle speed and V_{wind} is the wind speed, both in m/s . The friction force offered by the tires is:

$$F_{rr} = M_v \cdot g \cdot \mu_{rr} \cdot \cos(\beta) \quad (3)$$

In (3), M_v is the total mass of the vehicle in kg , g is the acceleration of gravity in m/s^2 , μ_{rr} is the dynamic friction coefficient and β is the slope angle of the track in degrees. The coefficient of dynamic friction can be estimated according to:

$$\mu_{rr} = \frac{k_1}{100} \cdot (5,1 + k_2 + k_3) \quad (4)$$

Where k_2 and k_3 can be determined respectively by (5) and (6).

$$k_2 = \frac{5,5 + 9 \cdot MVR \cdot 10^{-2}}{P_{PNEU}} \quad (5)$$

$$k_3 = \frac{8,5 + 3 \cdot MVR \cdot 10^{-2}}{P_{PNEU}} \cdot \left(\frac{V_x - V_{wind}}{100} \right) \quad (6)$$

The constant k_1 in (4), is the coefficient of tire pressure, that varies depending on the type of tire, in the case of radial tires it is 0,8, P_{PNEU} is the tire pressure in kPa , MVR is the mass of the vehicle loaded per wheel in kg , V_x and V_{wind} in this expression are given in km/h . The resistant force due to the slope of the track can be calculated as in (7):

$$F_{Incl} = M_v \cdot g \cdot \sin(\beta) = M_v \cdot g \cdot [(h \cdot 100)/c] \quad (7)$$

In (7), h is the height of the unevenness and the constant c is the standardized length of the ramp (c is equal to 100 meters). Table II presents the percentage slope value obtained for an angle β of 3° .

TABLE II
TRACK SLOPE β

Angle β	Slope (%)
3°	5,23

The resistant force in N , due to the acceleration of the vehicle can be calculated according to:

$$F_{accel} = M_v \cdot \frac{d}{dx}(V_x) \quad (8)$$

Since it is an elastic tire, for the tire-track contact force to occur, there must be a slip s not null, so that the coefficient of friction varies depending on this slip, that is, $u_{rr} = f(s)$. So the slip s can be obtained by:

$$s = \left| \frac{r_d \cdot \omega - V_x}{r_d \cdot \omega} \right| \quad (9)$$

Fig. 5 illustrates the behavior of static and dynamic friction coefficients as a function of slip.

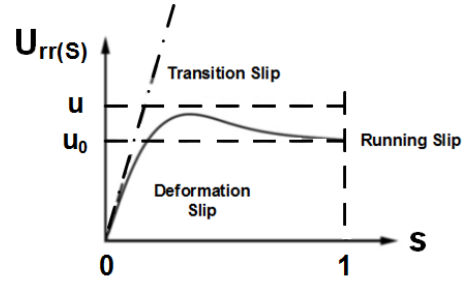


Fig. 5. Behavior of static and dynamic friction coefficients.

The parameter r_0 , in Fig. 6, is the radius of the wheel without deformation, r is the radius of the deformed wheel, r_d is the effective wheel radius, e_{DIANT} is the displacement of the normal force point and F_{ZDIANT} is the normal component of the force.

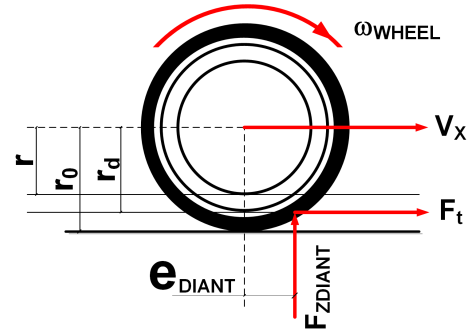


Fig. 6. Detail of the Wheel.

Tire deformation can be estimated in (10):

$$\rho = r_0 - r \quad (10)$$

The effective radius of the wheel can be approximated by:

$$r_d = r_0 - \left(\frac{\rho}{3} \right) \quad (11)$$

Due to the tire deformation, the contact point force of the wheel to the ground undergoes a displacement from the center of the wheel. Thus, the traction force can be obtained by the coefficient of dynamic friction and the normal force exerted on the front wheel.

$$F_t = F_{ZDIANT} \cdot \mu_{rr} \quad (12)$$

In this way, the total resistant power P_R , obtained by (1), can be determined by (13).

$$P_R = F_t \cdot V_x \quad (13)$$

Thus, the resistant torque is calculated according to (14):

$$T_R = P_R / \left(\frac{V_x \cdot 30 \cdot 0,104}{\pi \cdot r_d} \right) \quad (14)$$

For resistant force calculation, resistant power and resistant torque, a conventional passenger vehicle for educational purpose was considered. Table III shows the general vehicle data and Fig. 7 illustrates the vehicle used for track test respectively.

TABLE III
DIDACTIC VEHICLE DATA

Parameter	Quantity	Units
Vehicle Mass (M_v)	650	kg
Front Area (A_f)	1,76	m^2
Aerodynamic Drag Coefficient (C_d)	0,48	-
Dynamic Friction Coefficient (μ_{rrr})	0,0107	-
Height of the Center of Gravity ($h_{C.G.}$)	0,5	m
Regime Speed (V_F)	30	km/h
Radius of the Wheel with deformation - (r_d)	0,3	m
Mass per Wheel (MVR)	162,5	kg
Acceleration Time (t_{acel})	30	s
Track Slope Angle (β)	3	degrees



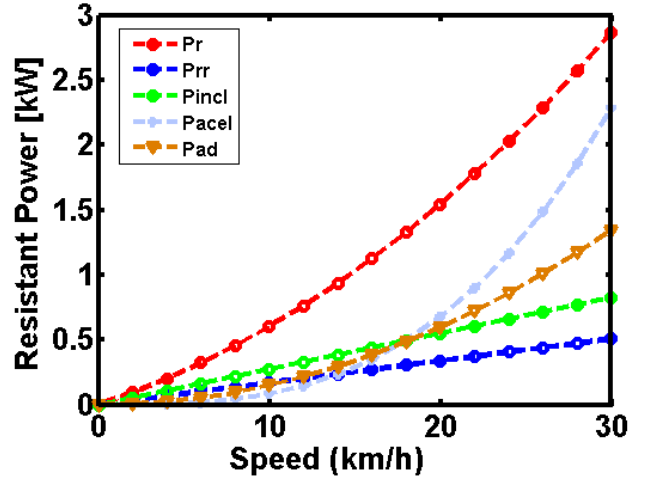
Fig. 7. Detail of vehicle used.

From data in Table III, it is possible to obtain the power and torque behavior, respectively, as depicted in Fig. 8a and Fig. 8b.

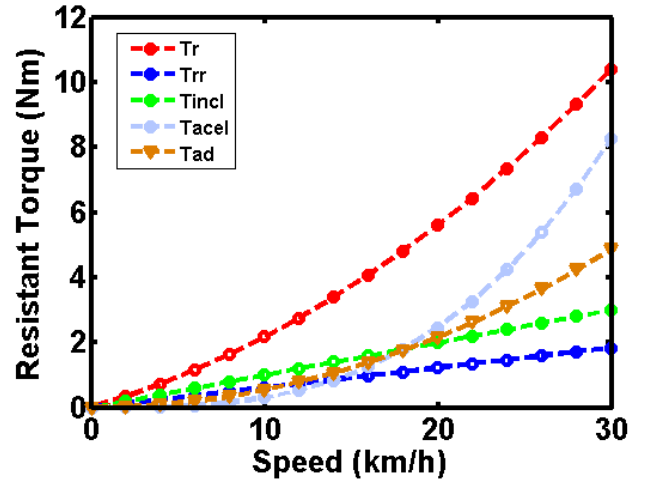
V. ELECTRIC MOTOR SIZING

The AFBPM machine specifically [16], does not require the use of commutators and carbon brushes regarding the excitation system [17]. The design and construction of a machine with this particular topology, consists as a first step, the sizing [18] through the resolution by analytical method as function of rated data as well as through the an equivalent magnetic circuit. The second step, a numerical solution by finite element method through the electromagnetic simulation software [19]–[21]. The third step consists of manufacturing of the 3 kW prototype based on the two previous steps. Firstly the size of the armature and rotor discs are calculated. From these dimensions it is possible to estimate the electromagnetic torque developed. As a starting point, the torque [22] derived from the differential torque expression was used in (15):

$$dT_d = \vec{\sigma} \otimes d\vec{S} \cdot r \quad (15)$$



(a) Resistant Power Components.



(b) Resistant Torque Components.

Fig. 8. Resistant Power and Torque for conditions in Table III.

In (15) $\vec{\sigma}$ is the shear stress vector in N/m^2 , $d\vec{S}$ is the area differential vector of the disc in m^2 and r is the radius of the disc in m . Fig. 9 presents the disk dimensions and the vector quantities.

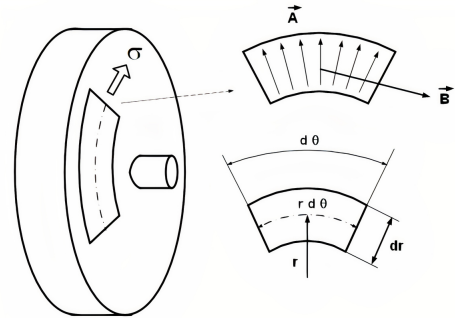


Fig. 9. Details of rotor dimensions and vector quantities.

The area differential element can be defined in terms of the differential arc and radius, thus, according to (16), results:

$$d\vec{S} = r \cdot d\vec{r} \cdot d\vec{\theta} \quad (16)$$

Through (15) and (16), the differential developed torque, can be determined by (17), becomes:

$$d\vec{T}d = \vec{\sigma} \otimes r^2 \cdot d\vec{r} \cdot d\vec{\theta} \quad (17)$$

Integrating (17), the developed torque can be calculated, according to (18):

$$\int_{R_{IN}}^{R_{OUT}} \int_0^{2\pi} dTd = \int_{R_{IN}}^{R_{OUT}} \int_0^{2\pi} \sigma \cdot r^2 \cdot dr \cdot d\theta \quad (18)$$

Solving (18) results:

$$Td = \frac{2\pi \cdot \sigma \cdot (D_{OUT}^3 - D_{IN}^3)}{24} \quad (19)$$

Considering factor K_d as a relationship between the internal and external diameters of the armature, in terms of D_{IN} :

$$D_{IN} = D_{OUT} \cdot K_d \quad (20)$$

By replacing (20) in (19) and putting in terms of D_{OUT} , the developed torque can be determined by:

$$Td = \frac{2\pi \cdot \sigma \cdot (1 - (K_d)^3) \cdot (D_{OUT})^3}{24} \quad (21)$$

Tangential stress σ is the cross product, point by point, between air gap flux density B , produced by the excitation system and the linear electric current density A produced by the armature, that is:

$$\sigma = B \cdot A \quad (22)$$

Replacing (22) in (21) and in the air gap, assuming a sinusoidal field distribution as well as the winding current, for 1 disk, results:

$$Td = \frac{\sqrt{2}\pi}{24} \cdot B_{MAX} \cdot A_{EFICAZ} \cdot (1 - K_d^3) \cdot (D_{OUT})^3 \quad (23)$$

Fig. 10 illustrates the dependence of the electromagnetic developed torque as a function of 3 different values of linear current densities and the outer radius of the disc for a maximum air gap flux density of 0.65 T [23].

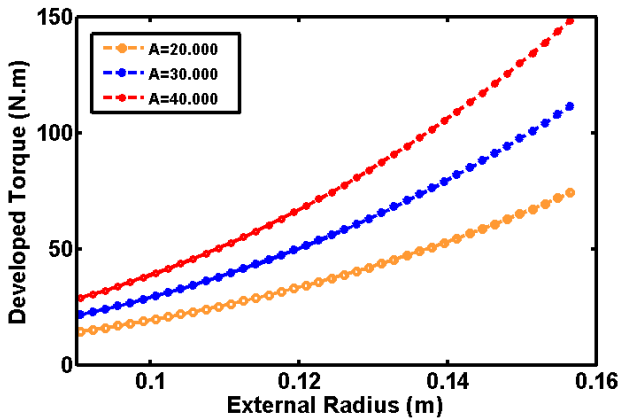


Fig. 10. Torque developed as a function of external radius for different linear current densities with constant induction.

In (23) D_{OUT} is the outer diameter of the disk in m , the constant A_{EFICAZ} is the effective linear current density in

$A \cdot turns/m$, the term B_{1MAX} is the maximum air gap flux density in T . Therefore, based on (23), the outer diameter of the disk can be determined according to (24).

$$D_{OUT} = \sqrt[3]{\frac{Td \cdot 24}{\sqrt{2} \cdot \pi \cdot B_{1MAX} \cdot A_{EFICAZ} \cdot (1 - K_d^3)}} \quad (24)$$

The SSAFBPM machine topology used in this project can be seen in Fig. 11. Fig. 11a, the concentrated toroidal armature winding and Fig. 11b, the permanent magnets arrangement on the rotor surface respectively.

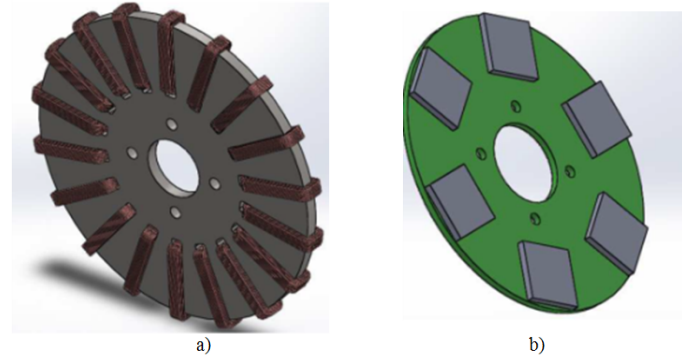


Fig. 11. a) Detail of the armature disk. b) Detail of the permanent magnet rotor.

Fig. 12 shows the flux lines paths produced by the permanent magnets and the simplified front view for magnetic circuit established among the armature, the air gap, the magnets and rotor. Through this circuit, the magnetic flux densities in the sections described above are determined.

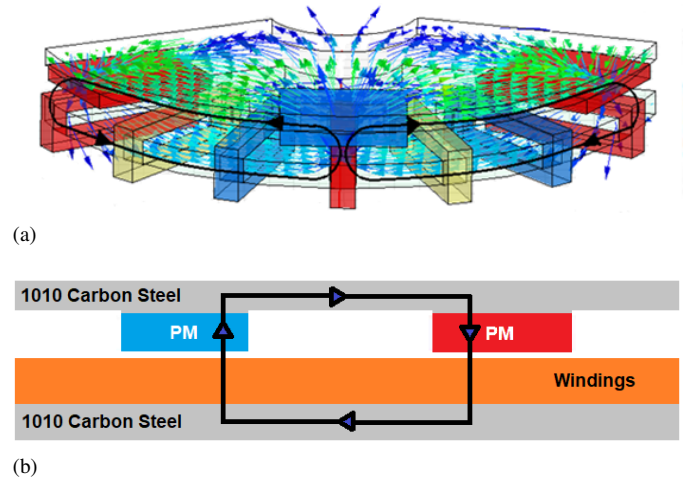


Fig. 12. Flux Paths Established by Permanent Magnets.

The total magnetomotive force produced by the permanent magnets [24] can be calculated by (25):

$$F_{PM} = \left(\sum_{n=1}^n Rn \right) \cdot \frac{\phi_{POLO}}{2} \quad (25)$$

Based on Fig. 12, given the reluctance due to each section, (25) can be rewritten as a function of reluctance of the air gap, stator and rotor, that is:

$$F_{PM} = (2 \cdot R_g + R_{EST} + R_{ROT}) \cdot \phi_{PM} \quad (26)$$

Where the magnetic reluctance of the stator and rotor becomes:

$$R = L_{MEDI0} \cdot (u \cdot S)^{-1} \quad (27)$$

In (27), L_{MEDI0} is the average length traveled by the magnetic flux, u is the permeability of the material and S is the cross section corresponding the flux passing through the stator and rotor parts. In this way, the flux density can be determined according to (28):

$$B = \frac{\phi_{PM}}{S} \quad (28)$$

The field intensity obtained from the magnetization curve visualized in Fig. 13 is:

$$H = B \cdot (u)^{-1} \quad (29)$$

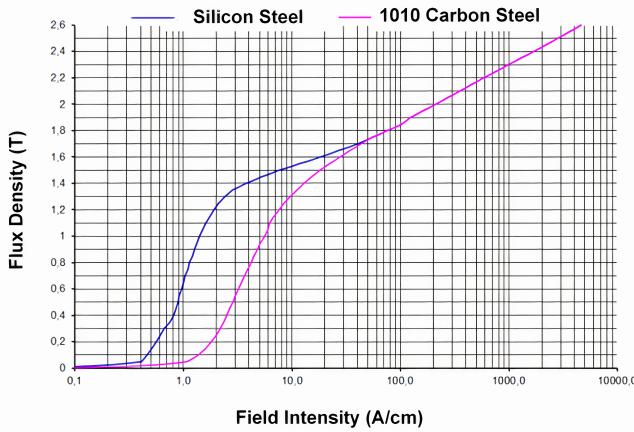


Fig. 13. Magnetization curve of the SAE 1010 Carbon Steel material.

The stator and rotor magnetomotive forces can be obtained from (30):

$$F = H \cdot L_{MEDI0} \quad (30)$$

The flux per pole can be determined according to (31):

$$\phi_{polo} = B_g \cdot S_P \quad (31)$$

In (31), S_P is the pole area, B_g is the air gap flux density. In the air gap, the magnetic reluctance becomes:

$$R_g = l_g \cdot (u_0 \cdot S_g)^{-1} \quad (32)$$

The parameter l_g in (32), is the length of the air gap and S_g is the air gap area. Thus, magnetomotive can be determined through:

$$F_g = B_g \cdot (u_0)^{-1} \cdot l_g \quad (33)$$

The air gap flux density in (33), can be calculated from the magnet operating curve, since its relative permeability has been determined [25], that is:

$$u_r = \frac{B_r}{H_c} \cdot \frac{1}{u_0} \quad (34)$$

In (34), B_r is the remanent flux density, H_c is the coercive magnetic field strength. In the rotor, sintered neodymium-iron-boron (NdFeB-35) square permanent magnets were used. Its characteristics are presented in table IV and depicted in Fig. 14.

TABLE IV
PM MAIN PARAMETERS

Parameter	Value
Remanent Flux Density (Br) - [T]	1,21
Coercive Field (Hc) - [A/m]	859 k

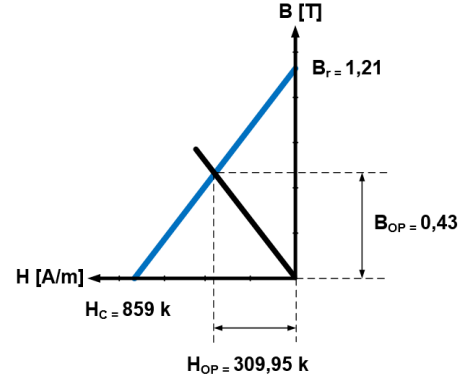


Fig. 14. Permanent Magnet BH Curve.

Therefore, the air gap flux density is calculated by

$$B_g = (B_r) / \left(\left(\frac{S_g}{S_{pm}} \right) + u_r \cdot \left(\frac{l_g}{l_{pm}} \right) \right)^{-1} \quad (35)$$

In (35) S_{pm} is the permanent magnet area in mm^2 and l_{pm} is the length of the permanent magnet in mm . Table V presents the rated data of the prototype and table VI the dimensions obtained through (15) to (35). In order to make possible operation at rated speed of 1200 rpm, the permanent magnet excitation system must produce a B_g of 0.65 T. In this project, the air gap length as well as the rotor depth were fixed. The B_g depends on the operation point from the permanent magnet curve. For this, firstly, the relative permeability value is determined, according to (36):

$$u_r = \frac{1,21}{859 \text{ k}} \cdot \frac{1}{u_0} = 1,120 \quad (36)$$

Thus, for an B_g of 0.65 T, the area of the permanent magnet, in mm^2 can be determined through (37):

$$0,65 = \frac{1,21}{\frac{3893,6}{S_{pm}}} + 1,120 \cdot \left(\frac{2,0}{6,35} \right)^{-1} = 2580,6 \quad (37)$$

The magnet dimensions, in millimeters, respectively are 50.8 x 50.8 x 6.35. Therefore, the operation flux density of the magnet is:

$$B_{OP} = 0,65 \cdot \frac{3893,6}{2580,6} = 0,43 \text{ T} \quad (38)$$

Considering the operation of the magnet at the maximum energy point, the coercive magnetic field strength is 309.95 k A/m. Based on Fig. 12, Table V and Table VI, flux densities, field strengths and magnetomotive force results, in each part of the topology are presented in Table VII.

TABLE V
MOTOR RATED VALUES

Quantity	Value
Rated Power [<i>kW</i>]	3
Rated Voltage [<i>V</i>]	220
Number of Phases [<i>m</i>]	3
Rated Speed [<i>rpm</i>]	1200
Rated Speed [<i>rps</i>]	20
Number of Poles	6
Rated Frequency [<i>Hz</i>]	60
Rated Current [<i>A</i>]	8,75
RMS Electric Current Density (A_{EF})	10155
Maximum AirGap Flux Density (T)	0,65
Voltage Factor	0,9
Form Factor	$2/\pi$
Concentrated Winding Factor	1
Efficiency adopted (η)	0,9
Power Factor adopted ($\cos \phi$)	1
AirGap length (l_g) [<i>mm</i>]	1
Armature and Rotor Material	1010 Carbon Steel

TABLE VI
MAIN MOTOR PARAMETERS

Parameter	Value
Armature D_{OUT} [<i>mm</i>]	260
Armature D_{IN} [<i>mm</i>]	150
Wire (AWG)	18
Total Number of Coils	18
Number of Turns per Coil	15
Parallel Paths	4

TABLE VII
ELECTROMAGNETIC QUANTITIES OBTAINED FROM FIG. 12

Section	B (T)	H (A.turns/cm)	L_{MEDIO} (cm)	F (A.turns)
Armature	0,98	5,40	10,73	57,95
Rotor	1,38	12,12	10,73	130,08
Air Gap	0,65	5,1725 k	0,2	1034,5
PM	0,43	85,9 k	0,635	54,5 k

VI. FINITE ELEMENT METHOD SIMULATION

Fig. 15 illustrates the flowchart over the methodology used for solving by numerical method, where the main steps were presented.

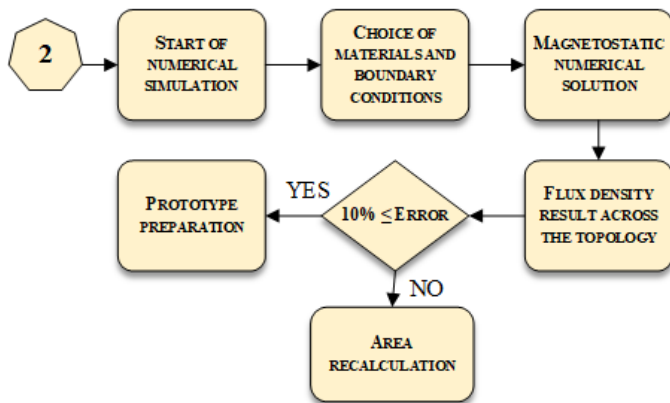


Fig. 15. Flowchart of Numerical Method.

Fig.16 show the simulation results by finite element method in magnetostatic regime in the stator (a) and rotor (b) respectively using Ansys Maxwell 13 software, where a color gradient represents the flux density.

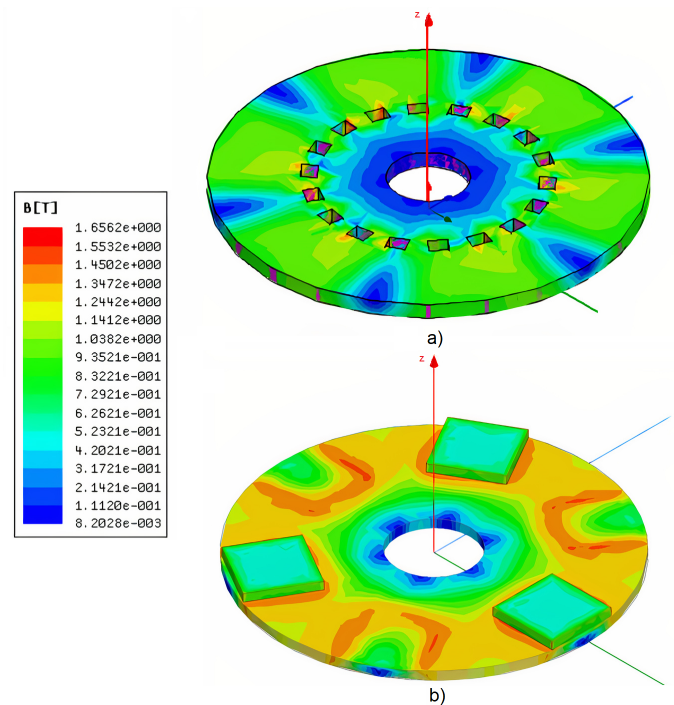


Fig. 16. Armature and Rotor Flux Density.

Fig. 17 and Fig. 18 shows the exploratory line for sampling the air gap flux density and the waveform obtained respectively.

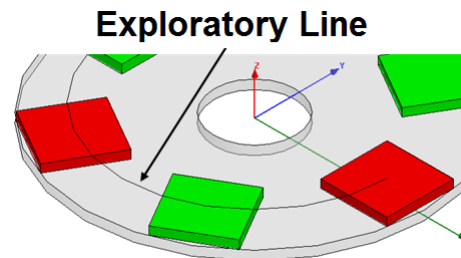


Fig. 17. Exploratory Line.

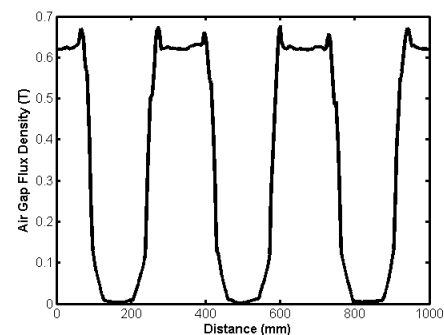


Fig. 18. Absolute Air Gap Flux Density - captured from exploratory line.

Fig. 19 illustrates the line voltage and armature current waveforms of the machine.

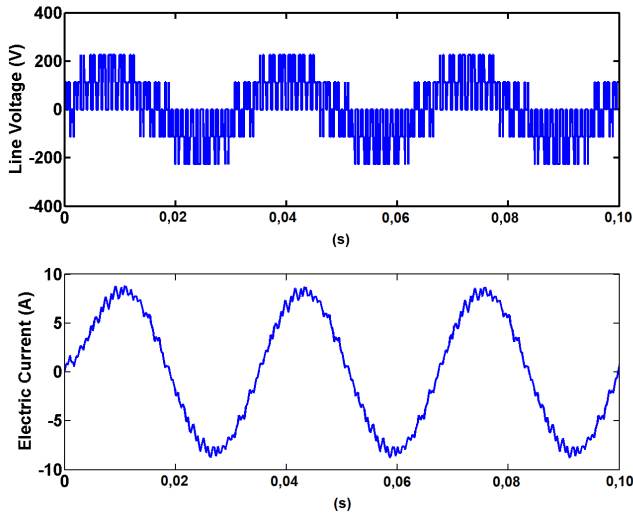


Fig. 19. Voltage and Current Armature.

VII. RESULTS

Table VIII presents the analytical and simulated magnetic induction levels and table IX, the analytical and simulated developed torque values are highlighted. In this way, the results has an error of nearly 5%. From Fig. 20 it can be seen the prototype manufactured from the analytical and numerical results and the test bench.

TABLE VIII
FLUX DENSITIES - RESULTS

Section	Analytical [T]	Simulation [T]	Perc Abs Error [%]
Armature	0,98	0,93 - 1,03	5,10
Rotor	1,38	1,25 - 1,35	2,17
Air Gap	0,65	0,62	4,61
PM	0,43	0,42 - 0,52	2,32

TABLE IX
DEVELOPED TORQUE RESULTS

Quantity	Td [N.m] Analytical	Td [N.m] Simulation	Perc Abs Error [%]
Developed Torque	13,80	12,50	9,42

The results of the bench tests are presented in the table X and XI respectively.

TABLE X
BENCH TEST RESULTS

f [Hz]	I [A]	N [rpm]	Td [N.m]
10	1,54	182	2,10
20	3,05	410	3,86
30	4,56	585	6,15
40	6,07	792	8,12
50	7,58	1030	10,34
60	9,1	1200	11,12

VIII. DISCUSSION AND CONCLUSIONS

In this work, a comparison between analytical and numerical method (via finite element method) was performed for the

TABLE XI
BENCH TEST RESULTS AND SIMULATION

Quantity	Simulation	Bench Test	Perc Abs Error [%]
Td [N.m]	12,50	11,12	11,04
Ia [A] (true rms)	8,75	9,10	4,00

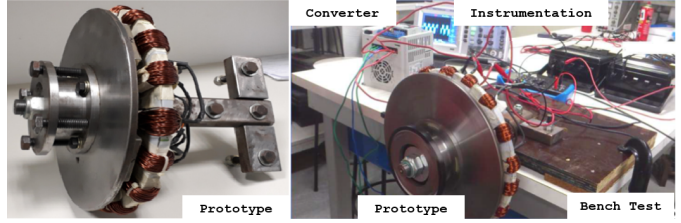


Fig. 20. Detail of the Prototype and Bench Test.

development of a brushless axial flux machine with a focus on the use in electric traction of a passenger vehicle for teaching purposes up to a speed of 30 km/h. The flux densities levels obtained in all parts of the device, through analytical and numerical methodology, have very similar values, in addition to the fact that they indicate no magnetic saturation in any part, a fact that would compromise the motor operation. Additionally, the torque values obtained in the 3 methods have a percentage error of 9.42 % between the analytical and simulated method, as well as a percentage error of 11.04 % between the simulated method and that obtained from the bench test validating the methodology. For this power range, a radial topology machine could easily be used to replace the internal combustion engine, given that space available in this vehicle for educational purposes does not restrict the use of a radial machine, however, its rear cover it is very close to the car's engine cover, practically leaning against it. The use of AFBPM machines is strongly justified only in places where the axial space is really reduced for a specific power, for instance in wheels of electric or hybrid vehicles, and in these places, SSAFBPM topology is most recommended. In vehicles with other traction system configurations and different power ranges (figure 2) axial motors can be used as long as the axial length is in fact compromised.

REFERENCES

- [1] A. N. Patel, B. N. Suthar, T. H. Panchal, and R. M. Patel in *2018 2nd IEEE International Conference on Power Electronics, Intelligent Control and Energy Systems (ICPEICES)*.
- [2] S. Wathage, C. Chen, and C. H. Perry, "Analysis of single side axial flux brushless dc motor with different number of stator electromagnetic poles," in *2012 Proceedings of IEEE Southeastcon*, pp. 1–6, 2012.
- [3] A. Echle, A. Neubauer, and N. Parspour, "Design and comparison of radial flux and axial flux brushless dc motors for power tool applications," in *2018 XIII International Conference on Electrical Machines (ICEM)*, pp. 125–130, 2018.
- [4] J. Lai, J. Li, and T. Xiao, "Design of a compact axial flux permanent magnet machine for hybrid electric vehicle," *IEEE Transactions on Industrial Electronics*, vol. 68, no. 8, pp. 6630–6639, 2021.
- [5] M. Fasil, N. Mijatovic, B. B. Jensen, and J. Holboll, "Finite-element model-based design synthesis of axial flux pmbldc motors," *IEEE Transactions on Applied Superconductivity*, vol. 26, no. 4, pp. 1–5, 2016.
- [6] L. Jia, M. Lin, N. Li, W. Le, X. Wu, and Z. Chen, "Magnetic equivalent circuit framework for an axial flux permanent magnet synchronous machine," in *2019 22nd International Conference on Electrical Machines and Systems (ICEMS)*, pp. 1–5, 2019.

- [7] P. Lindh, J. Montonen, H. Jussila, J. Pvrhonen, W. Jara, and J. Tapia, "Axial flux machine structure reducing rotor eddy current losses," in *IEEE International Electric Machines and Drives Conference*, pp. 143–146, 2015.
- [8] A. Fuhs, *Hybrid Vehicles and the Future of Personal Transportation*. CRC Press, 2009.
- [9] L. Belkacem, H. Mustapha, K. Katia, and G. Ahmed, "Design and investigation of axial flux permanent magnet synchronous machine for electric vehicles," in *2018 International Conference on Communications and Electrical Engineering (ICCEE)*, pp. 1–6, 2018.
- [10] Q. Wang, F. Zhao, and K. Yang, "Analysis and optimization of the axial electromagnetic force for an axial-flux permanent magnet vernier machine," *IEEE Transactions on Magnetics*, vol. 57, no. 2, pp. 1–5, 2021.
- [11] B. Zhang, T. Epskamp, M. Doppelbauer, and M. Gregor, "A comparison of the transverse, axial and radial flux pm synchronous motors for electric vehicle," in *2014 IEEE International Electric Vehicle Conference (IEVC)*, pp. 1–6, 2014.
- [12] Y. Chen, W. N. Fu, S. L. Ho, and H. Liu, "A quantitative comparison analysis of radial-flux, transverse-flux, and axial-flux magnetic gears," *IEEE Transactions on Magnetics*, vol. 50, no. 11, pp. 1–4, 2014.
- [13] A. Chen, R. Nilsen, and A. Nysveen, "Performance comparisons among radial flux, multistage axial flux, and three-phase transverse-flux PM machines for downhole applications," vol. 46, pp. 779–789, 2010.
- [14] M. Ehsani, Y. Gao, and A. Emadi, *Modern Electric, Hybrid Electric and Fuel Cells Vehicles*. CRC Press, 2010.
- [15] A. Pelizari and I. E. Chabu, "Fem analysis of a non-conventional axial flux hybrid excitation motor under flux weakening operation for electric vehicle purpose," in *2015 International Conference on Electrical Systems for Aircraft, Railway, Ship Propulsion and Road Vehicles (ESARS)*, pp. 1–6, 2015.
- [16] J. F. Gieras, R. Wang, and M. J. Kamper, *Axial Flux Permanent Magnet Brushless Machines*. Kluwer, 2004.
- [17] F. Caricchi and F. Crescimbin, "Axial-flux permanent-magnet machine with water-cooled ironless stator," in *Proc. IEEE Power Tech Conf.*, vol. 4, pp. 98–103, 1995.
- [18] H. Bali, Y. Amara, G. Barakat, R. Ibtouen, and M. Gabsi, "Analytical Modeling of Open Circuit Magnetic Field in Wound Field and Series Double Excitation Synchronous Machines," *IEEE Transactions on Magnetics*, vol. 46, pp. 3802–3815, 2010.
- [19] C. C. Chan, "Axial-field electrical machines: Design and application," *IEEE Trans. Energy Conversion*, vol. 2, p. 294, 1987.
- [20] H. Y. Lv, X. Y. Wang, J. J. Du, and L. H. Zhu, "Analytical calculation of pmsg optimization for compact er-eps application," in *2015 IEEE International Conference on Applied Superconductivity and Electromagnetic Devices (ASEMD)*, pp. 551–552, 2015.
- [21] P. Ojaghlu and A. Vahedi, "A new axial flux permanent magnet machine," *IEEE Transactions on Magnetics*, vol. 54, no. 1, pp. 1–6, 2018.
- [22] S. Huang, J. Luo, F. Leonardi, and T. A. Lipo, "A general approach to sizing and power density equations for comparison of electrical machines," vol. 34, pp. 92–97, 1998.
- [23] M. Cirani, C. Sararangani, and P. Thelin, "Analysis of an innovative design for an axial flux torus machine," in *Proc. ICEM*, p. 151, 2002.
- [24] F. Caricchi, F. Crescimbin, F. Fedeli, and G. Noia, "Design and construction of a wheel-directly-coupled axial-flux pm motor prototype for eps," in *Proc. IEEE-IAS Annu. Meeting*, p. 254, 1994.
- [25] T. F. Chan, W. Wang, and L. L. Lai, "Performance of an axial-flux permanent magnet synchronous generator from 3-D finite-element analysis," *IEEE Trans. Energy Conv.*, vol. 25, pp. 669–676, 2010.
- [26] Y.-C. Chang, J.-T. Chan, J.-C. Chen, and J.-G. Yang, "Development of permanent magnet synchronous generator drive in electrical vehicle power system," in *2012 IEEE Vehicle Power and Propulsion Conference*, pp. 115–118, 2012.
- [27] S. Neethu, S. Nikam, B. Fernandes, S. Pal, and A. Wankhede, "Radial- and axial-flux synchronous motors for high-speed low-power applications," in *2018 IEEE International Conference on Power Electronics, Drives and Energy Systems (PEDES)*, pp. 1–4, 2018.
- [28] A. Loganayaki and R. B. Kumar, "Permanent magnet synchronous motor for electric vehicle applications," in *2019 5th International Conference on Advanced Computing Communication Systems (ICACCS)*, pp. 1064–1069, 2019.
- [29] P. Dück, P. Lesniewski, and B. Ponick, "Design and analysis of axial-flux permanent magnet synchronous machines as traction drives for electric vehicles," in *2016 International Symposium on Power Electronics, Electrical Drives, Automation and Motion (SPEEDAM)*, pp. 376–381, 2016.



Ademir Pelizari is an electrical engineer graduated from the University of Mogi das Cruzes (UMC), São Paulo, Brazil in 2002. He completed his master's and doctoral degrees in 2009 and 2015, respectively. He currently works as a Adjunct Professor at the Federal University of ABC (UFABC) in the areas of electromechanical devices and electrical machines.



Alfeu Joãozinho Sguarez Filho is Adjunct Professor at the Federal University of ABC (UFABC) with Doctor's degrees in Electrical Engineering from the Faculty of Electrical and Computer Engineering of the State University of Campinas (Unicamp) in 2007 and 2010, respectively. He is a Senior Member of the IEEE and researcher and author of several articles in national and international scientific journals and book chapters in the areas of electrical machines, machine control, power electronics, wind energy.



Gabriel Rodrigues Bruzinga is an electrical engineer graduated from the federal university of ABC (2018) and is currently in the postgraduate program with a master's degree in electrical engineering. The focus of the project involves the design of permanent magnet synchronous generators (PMSG) with a focus on wind energy.